The Astrophysical Journal, 617:623–632, 2004 December 10

WAVELET PHASE COHERENCE ANALYSIS: APPLICATION TO A QUIET-SUN MAGNETIC ELEMENT

D. Shaun Bloomfield,[1] R. T. James McAteer,[1,2] Bruce W. Lites,[3,4] Philip G. Judge,[3]
Mihalis Mathioudakis,[1] and Francis P. Keenan[1]

Received 2004 June 28; accepted 2004 August 16

ABSTRACT

A new application of wavelet analysis is presented that utilizes the inherent phase information residing within the complex Morlet transform. The technique is applied to a weak solar magnetic network region, and the temporal variation of phase difference between *TRACE* 1700 Å and *SOHO*/SUMER C II 1037 Å intensities is shown. We present, for the first time in an astrophysical setting, the application of wavelet phase coherence, including a comparison between two methods of testing real wavelet phase coherence against that of noise. The example highlights the advantage of wavelet analysis over more classical techniques, such as Fourier analysis, and the effectiveness of the former to identify wave packets of similar frequencies but with differing phase relations is emphasized. Using cotemporal, ground-based Advanced Stokes Polarimeter measurements, changes in the observed phase differences are shown to result from alterations in the magnetic topology.

Subject headings: methods: data analysis — Sun: chromosphere — Sun: magnetic fields — Sun: oscillations

Online material: color figures

1. INTRODUCTION

The nature of oscillations in quiet-Sun regions of the solar atmosphere has been studied extensively using Fourier techniques for a number of decades (early work is reviewed in Gibson 1973). Fourier power spectra clearly show that regions of "nonmagnetic" internetwork (supergranular cell interiors) are dominated by higher frequencies, $\nu > 4$ mHz, while the "magnetic" network (supergranular cell boundaries) is dominated by lower frequencies, $\nu < 4$ mHz (Lites et al. 1993). Through such Fourier work, Lites et al. (1993) found that both network and internetwork displayed well-correlated, coherent oscillations between the photosphere and low chromosphere (temperature minimum) for frequencies around those of the solar *p*-mode. In support of this, Judge et al. (2001) propose that the dynamics of the internetwork atmosphere are driven by high-frequency tails of the *p*-mode distribution. Meanwhile, Lites et al. (1993) also found that the internetwork remained coherent in the *p*-mode range between the low and mid-chromosphere, while the network displayed a lack of such coherence. As such, it appears that the presence of a more substantial magnetic field in the network acts to alter the oscillations seen in the chromosphere from those in the photosphere below.

It has been known for over 30 yr that solar *p*-mode oscillations are observed in 20–30 minute coherent "packets" (Gibson 1973). Studies of the power contained in a time series, consisting of a train of such packets, will result in essentially the same result whether looked at with either Fourier analysis (no timing information) or wavelet analysis (time-localized). This is because power is always a positive quantity; hence, averaging over time (analogous to the Fourier case) will only marginally lower the confidence level achieved. However, if the phase relations of the driving packets differ or a change occurs in the local topology (more likely for the network, e.g., through field line rearrangement due to reconnection events or emerging/submerging flux), Fourier analysis will more drastically "wash out" these relations over the duration of the observation. This is because phase is not necessarily positive but can take on negative values as well. Other forms of Fourier analysis (i.e., running windowed) can be utilized to gain temporal information akin to that achieved by wavelet analysis. However, choosing which size of temporal window to employ enters a degree of subjectivity to the analysis along with a number of problems, including decreased frequency resolution and a differing number of oscillations within the window for different frequencies.

In this paper we apply a wavelet phase coherence analysis to a quiet-Sun magnetic element. The layout of the paper is as follows. In § 2 we outline the observations used in this work, while the wavelet techniques employed are shown in § 3, with their application displayed and discussed in § 4. Finally, we present our conclusions in § 5.

2. DATA

The data analyzed here were obtained as part of Joint Observing Proposal 72 (JOP072) between the *SOHO* and *TRACE* satellites. In addition to the space-based data (*SOHO*/MDI, *SOHO*/SUMER, and *TRACE*), ground-based support was provided on 1998 May 16 from the Dunn Solar Telescope at Sacramento Peak, New Mexico. The latter included vector magnetograms taken with the High Altitude Observatory's Advanced Stokes Polarimeter (ASP) and rastered Ca II H line core and wing spectra. The spatial coverage of the ground-based observations is outlined in Figure 1 with respect to that obtained by the *SOHO* and *TRACE* satellites, while the ASP field of view (FOV), cospatial *TRACE* sub-FOV, and SUMER slit positioning are shown in greater detail in Figure 2.

The ASP records full Stokes spectra (I, Q, U, V) of the Zeeman-sensitive, photospheric Fe I 6301.5 and 6302.5 Å line

[1] Department of Pure and Applied Physics, Queen's University Belfast, Belfast BT7 1NN, Northern Ireland, UK; s.bloomfield@qub.ac.uk.
[2] NRC Research Associate, NASA Goddard Space Flight Center, Solar Physics Branch, Code 682, Greenbelt, MD 20771.
[3] High Altitude Observatory, National Center for Atmospheric Research, Boulder, CO 80307-3000.
[4] Visiting Astronomer, National Solar Observatory, operated by the Association of Universities for Research in Astronomy, Inc. (AURA), under cooperative agreement with the National Science Foundation.

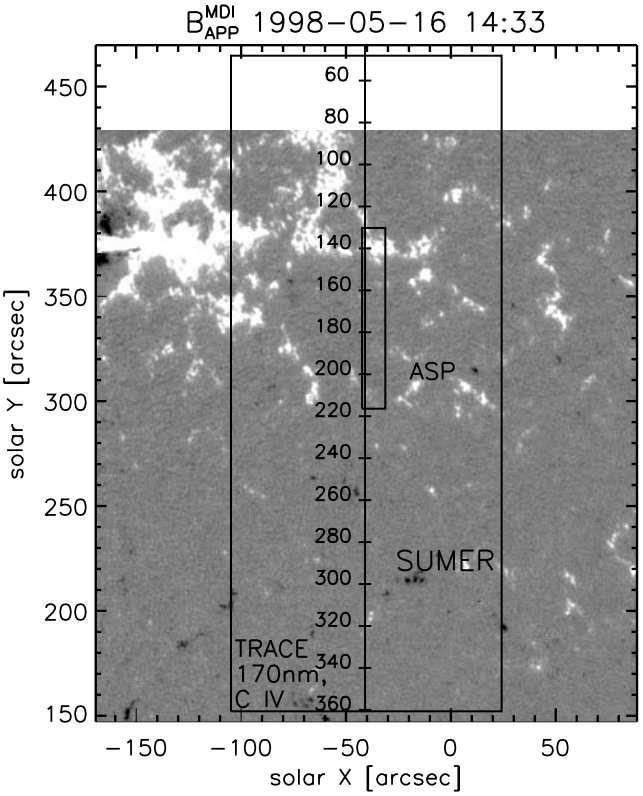

FIG. 1.—*SOHO*/MDI longitudinal magnetic field context image, taken shortly before the ground-based observations commenced. The extent of both the ASP and *TRACE* FOV coverages (bounded by small and large boxes, respectively) and the SUMER slit positioning are shown.

pair. Inversion of these spectra by nonlinear, least-squares fitting of synthesized Milne-Eddington model atmosphere profiles (Skumanich & Lites 1987) leads to the determination of the line-of-sight magnetic field, its directional vector components, and a number of atmospheric parameters, from which the apparent magnetic flux density at the photosphere can be calculated.

The JOP072 satellite data have been previously published in Judge et al. (2001), and the reader is directed to this paper for a detailed description of the observations and data alignment. Judge et al. (2001) mention that some possible network elements were only visible in the 1998 May 16 data set as persistently brighter streaks in the *TRACE* 1700 Å observations (starting at $x = 182$, 191 in their Figs. 3 and 4), as they were probably below the *SOHO*/MDI sensitivity level. In the present work we use the more sensitive ASP instrument to identify and isolate one of these elements.

For the purposes of this paper we use the (UV continuum–dominated) *TRACE* 1700 Å and SUMER C II 1037 Å emission line intensities. These are formed in the solar atmosphere close to the temperature minimum (1700 Å) and farther up in the lower transition region (C II). Although the ground-based data were recorded with slightly varying time separation, the ASP data were interpolated to a constant cadence (∼61 s) and the higher cadence *TRACE* and SUMER data (15 and 10–15 s, respectively) were also interpolated to this common, constant time base for comparative purposes. The pointing of the SUMER slit at each ASP time stamp was then determined (Fig. 2), and the SUMER slit region of the ASP and *TRACE* data extracted. Spacetime plots were constructed by stacking the regions extracted from successive images and are shown in Figure 3. It can be clearly seen in Figures 2 and 3 that regions of increased 1700 Å intensity closely follow regions of heightened photospheric magnetic flux. However, Figure 3 shows that the spatial correlation between increased intensity and magnetic flux has disappeared by the height of C II emission.

The magnetic element studied (shown in more detail in Fig. 4) can be seen starting near $x = 182$, before drifting along the slit with time. Light curves of the 1700 Å and C II intensities above this network element are displayed in Figure 5. These were obtained by averaging over a 4″ region along the slit, as marked out in Figures 3 and 4 by dashed lines. This region was centered on the weak flux element, thus tracking the element as it moved along the slit.

It is worth noting that around image 52 (time ≈ 53 minutes) a small, weak, magnetic flux emergence occurs close to the magnetic element studied. Before the end of the time series (image ∼ 90, time ≈ 92 minutes), this emergent flux moves away from the magnetic element under consideration and subsequently coalesces with another magnetic element.

3. WAVELET ANALYSIS

The main benefit of wavelet[5] over Fourier analysis is that both time and frequency localization can be achieved in the former. This is because wavelet analysis employs a wave packet, whereas Fourier analysis uses an infinite wave train of sines and cosines. In recent years wavelet power transforms have become increasingly popular (e.g., De Moortel et al. 2000; Williams et al. 2001; Bloomfield et al. 2004), while the additionally available phase information has remained untapped—an exception being a recent paper by De Pontieu et al. (2003), which reports wavelet phase difference values but includes no work on phase coherence.

Here we use the standard Morlet wavelet: a Gaussian modulated sine wave of the form (Torrence & Compo 1998)

$$\psi(\eta) = \pi^{-1/4} \exp(i\omega_0\eta) \exp\left(-\frac{\eta^2}{2}\right), \qquad (1)$$

where $\pi^{-1/4}$ is a normalization term, $\eta = n/s$ is the dimensionless time parameter, n is the time parameter, s is the scale of the wavelet, $\omega_0 = s\omega$ is the dimensionless frequency parameter (taken as $\omega_0 = 6$ for this work), and ω is the frequency parameter. It should be noted that in wavelet analysis the wavelet scale is directly related to the oscillation period ($P = 1.03s$ for the Morlet wavelet) and hence oscillation frequency. We note that an infinite number of mother wavelets are available, including the derivative-of-a-Gaussian (DOG) and Paul wavelets. We choose the complex Morlet wavelet as it yields a complex wavelet transform, containing information on both amplitude and phase. Since DOG wavelets are entirely real, they may not be used for phase analysis, as their real transforms hold only information on amplitude. Alternatively, the complex Paul wavelet could be employed. However, as the Paul function is more sharply defined in time (in comparison to the more sinusoidal Morlet function), it is better suited for studying pulse-like variations.

The equations describing the wavelet transform and its Fourier equivalent are depicted in Table 1. Typical wavelet power transforms are shown in Figures 6*a* and 6*b* for the 1700 and C II 1037 Å intensity time series, respectively. In these and

[5] Wavelet software was provided by C. Torrence and G. P. Compo and is available at http://paos.colorado.edu/research/wavelets.

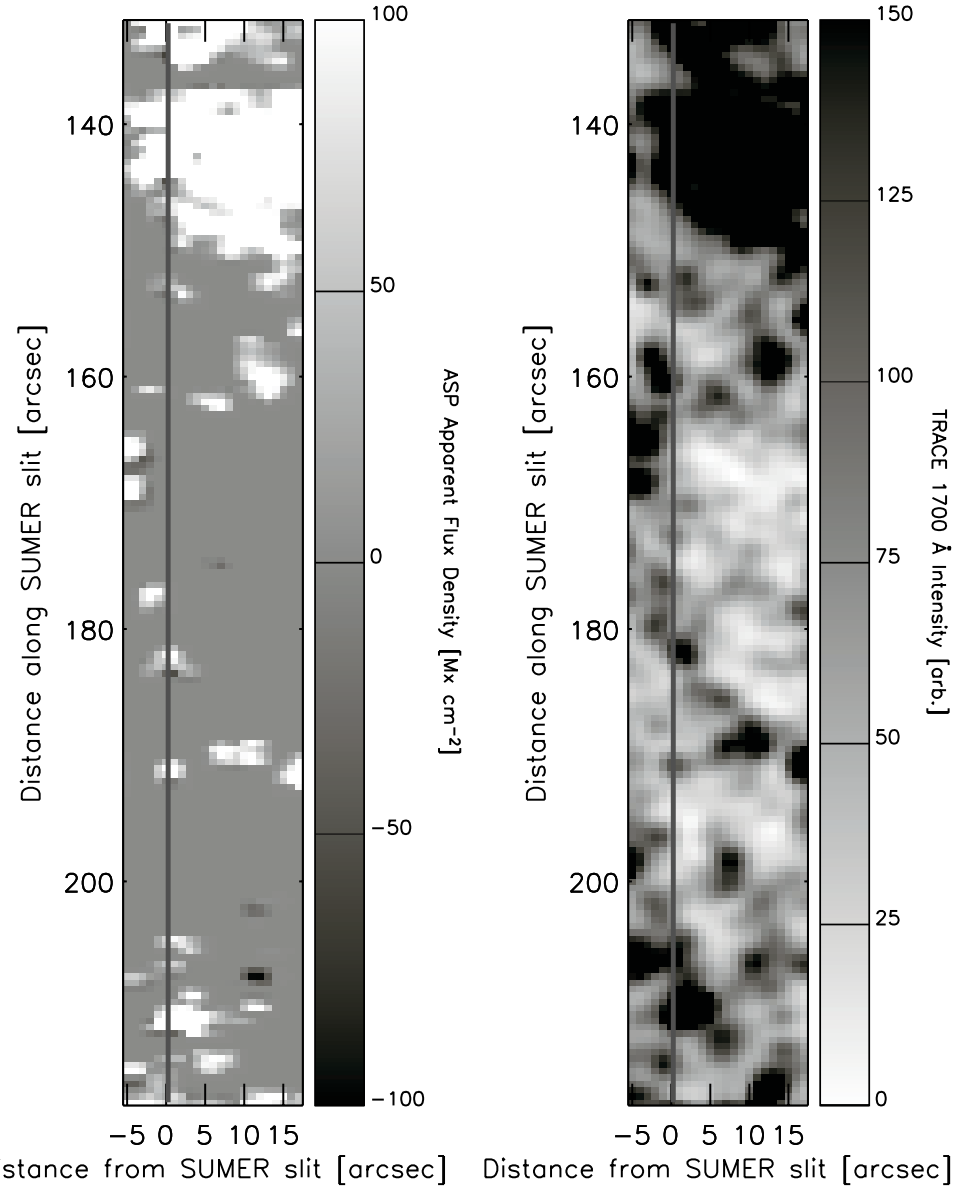

FIG. 2.—Examples of both the ASP and *TRACE* FOV from the start of the time series, with the SUMER slit superposed as a solid vertical line. Both images have been clipped to show fine details. [*See the electronic edition of the Journal for a color version of this figure.*]

the following power plots, lighter shading indicates regions of increased power, while the crosshatched areas correspond to the cone of influence (COI), where edge effects may become important because of the finite duration of the time series. Also marked on these plots are contours of the 95% confidence levels, as determined from a 2 degree of freedom χ^2 distribution.

3.1. *Cross-Wavelet Transform*

The cross–wavelet transform between two time series is simply the multiplication of the first complex wavelet transform with the complex conjugate of the second, again shown in Table 1. From this complex cross–wavelet transform, the power $|W_n^{XY}(s)|$ and individual real, $\mathcal{R}$, and imaginary, $\mathcal{I}$, components are involved in determining both the wavelet phase coherence and the wavelet phase difference.

While a wavelet power spectrum depicts the variance of a time series, with times of large variance showing large power, the cross–wavelet power of two time series depicts the covariance between these time series. Additionally, cross–wavelet power has a known distribution of confidence levels, which is proportional to the square root of the product of two χ^2 distributions (Torrence & Compo 1998). This allows cross–wavelet power to be used as a quantified indication of the similarity of power between two time series. The cross–wavelet power transform associated with the two individual power transforms depicted in Figures 6*a* and 6*b* is displayed as Figure 6*c*.

3.2. *Phase Coherence*

The measuring of phase coherence is carried out to attribute a value of support to measurements of phase difference between two time series, with large values of phase coherence signifying that the phase difference varies smoothly as a function of frequency (i.e., nonrandom). As such, Torrence & Webster (1999) describe wavelet coherency as "an accurate representation of the (normalized) covariance between the two time series."

The complex cross–wavelet transform is used to determine the wavelet phase coherence in the manner depicted in Table 1,

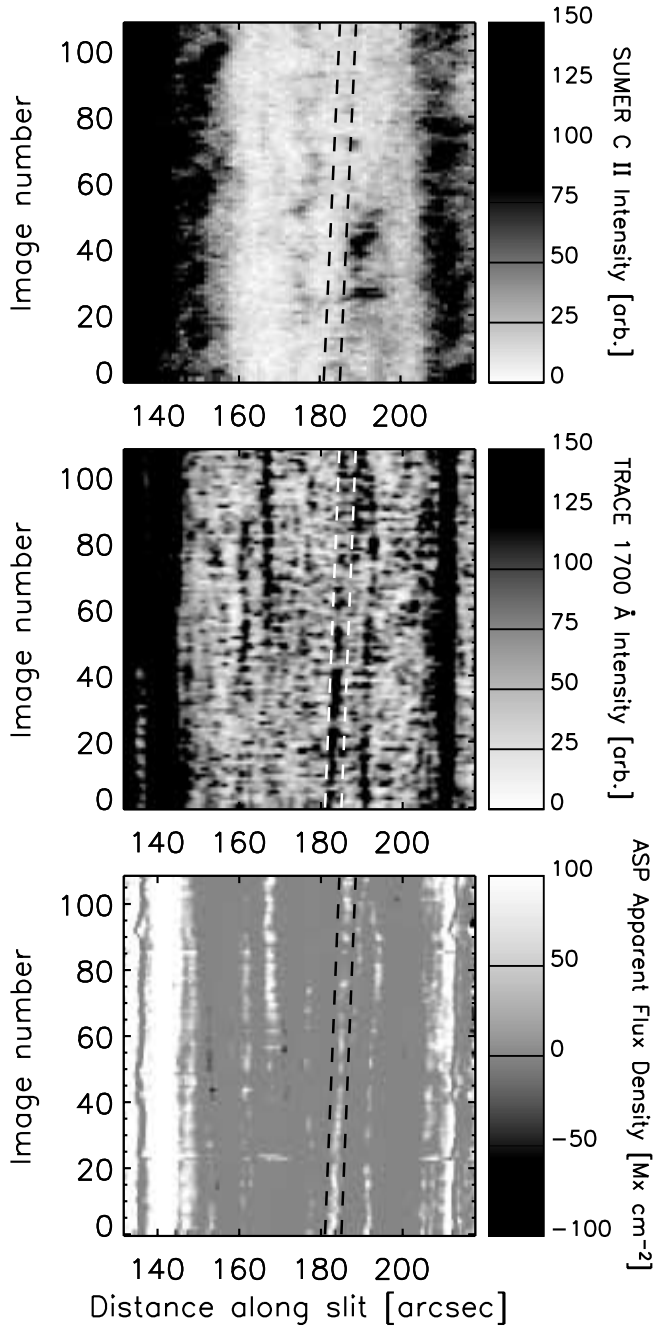

FIG. 3.—*Top*: SUMER C II 1037 Å intensity (in arbitrary units). *Middle*: *TRACE* 1700 Å intensity (in arbitrary units) below the projected SUMER slit. *Bottom*: Photospheric apparent magnetic flux density obtained with the ASP (in units of Mx cm^{-2}) below the projected SUMER slit. Plots are shown as a function of position along SUMER slit (*abscissa*) and image number (*ordinate*). Successive image numbers are separated in time by the ASP cadence (61 s). In all plots, ranges of intensity or flux have been clipped to help show fine detail, and the dashed lines mark the weak network element under consideration. [*See the electronic edition of the Journal for a color version of this figure.*]

where $\langle \cdots \rangle$ indicates smoothing in both time and scale. A Gaussian profile—identical to the Gaussian component of the Morlet wavelet but normalized to a weight of unity—was used for the smoothing in time,

$$\frac{1}{s\sqrt{2\pi}} \exp\left(-\frac{\eta^2}{2}\right), \tag{2}$$

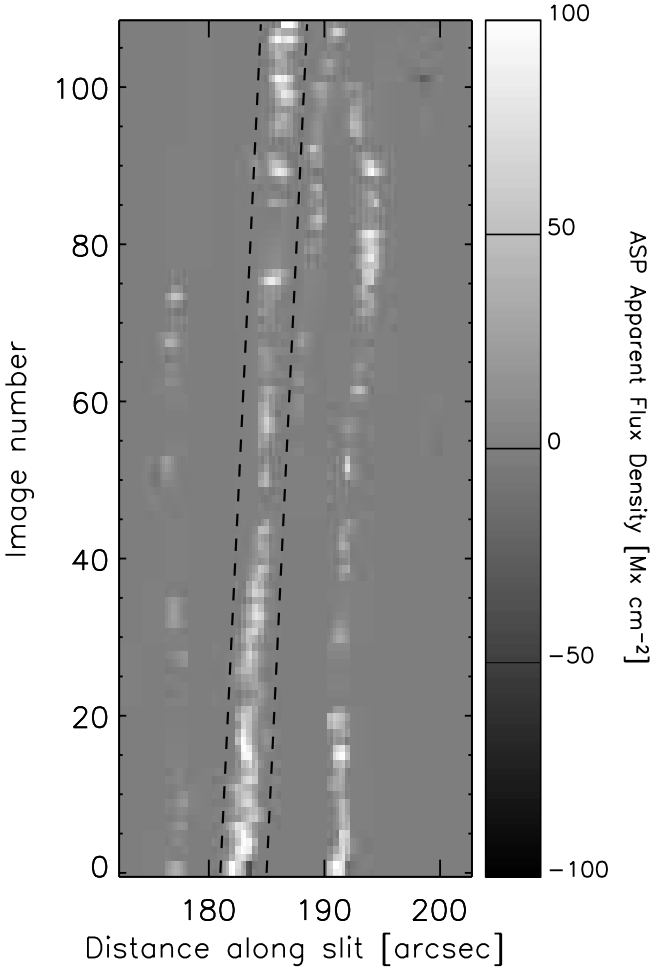

FIG. 4.—Expanded version of the bottom panel in Fig. 3, showing weak network elements in greater detail.

while smoothing in scale was carried out with a boxcar filter of width δj_0 (=0.6 for the Morlet case, taking in scale values over the range $0.7s \leq s \leq 1.3s$). These forms of smoothing are adopted as they effectively recreate the natural profiles of the Morlet wavelet function in both time and scale space. The smoothed $\mathcal{R}$ and $\mathcal{I}$ components of the cross–wavelet transform

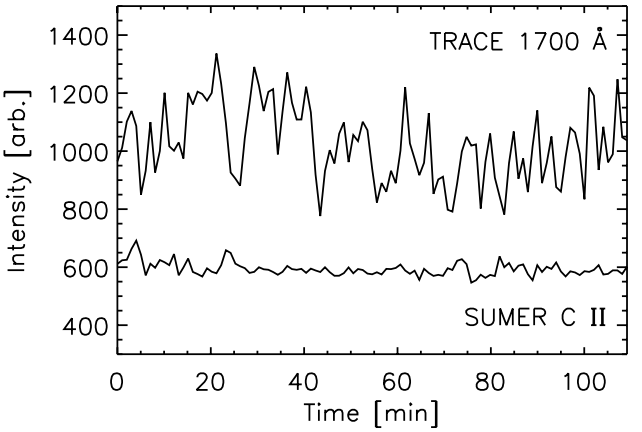

FIG. 5.—Projected SUMER slit time series of the *TRACE* 1700 Å and SUMER C II 1037 Å intensities. The C II values have been shifted upward by 500. [*See the electronic edition of the Journal for a color version of this figure.*]

TABLE 1
COMPARISON OF EQUATIONS USED IN WAVELET AND FOURIER ANALYSIS

Quantity	Wavelet Form[a]	Fourier Form[b]
Transform	$W_n(s) = \sum_{n'=0}^{N-1} x_{n'} \psi^* \left[\frac{(n'-n)\delta t}{s}\right]$	$F_j = \sum_{k=0}^{N-1} f_k \exp\left(-\frac{2\pi i j k}{N}\right)$
Cross-transform	$W_n^{XY}(s) = W_n^X(s) W_n^{Y*}(s)$	$F_j^{XY} = F_j^X F_j^{Y*}$
Phase coherence	$R_n^2(s) = \frac{\lvert\langle s^{-1} W_n^{XY}(s)\rangle\rvert^2}{\langle s^{-1}\lvert W_n^X(s)\rvert^2\rangle \langle s^{-1}\lvert W_n^Y(s)\rvert^2\rangle}$	$C_j^2 = \frac{\lvert\langle F_j^{XY}\rangle\rvert^2}{\langle\lvert F_j^X\rvert^2\rangle\langle\lvert F_j^Y\rvert^2\rangle}$
Phase difference	$\phi_n(s) = \arctan\left(\frac{\mathcal{I}\{\langle s^{-1} W_n^{XY}(s)\rangle\}}{\mathcal{R}\{\langle s^{-1} W_n^{XY}(s)\rangle\}}\right)$	$\Phi_j = \arctan\left(\frac{\mathcal{I}\{F_j^{XY}\}}{\mathcal{R}\{F_j^{XY}\}}\right)$

[a] The value n is the time; s is the scale of the wavelet ($P = 1.03s$ for the Morlet); $\eta = n/s$ is the dimensionless time parameter; $\omega_0 = s\omega$ is the dimensionless frequency parameter; and * signifies the complex conjugate (Torrence & Compo 1998; Torrence & Webster 1999).

[b] For a continuous signal sampled at N discrete points ($k = 0, 1, \ldots, N-1$), $f(t) \rightarrow f(t_k) \equiv f_k$ for $t_k \equiv k\delta t$. Hence, F_j corresponds to the Fourier transform at frequency $\nu_j = j/N\delta t$, where $j = -N/2, -(N/2)+1, \ldots, N/2$.

are used to construct the power of the smoothed cross–wavelet in the numerator. However, in the denominator the smoothing in both time and scale are applied after the powers of the first and second time series have been calculated. The s^{-1} factors in this equation are required to convert to an energy density (Torrence & Webster 1999).

It can be seen from Table 1 that wavelet phase coherence is analogous to that used in Fourier analysis. In the Fourier case it is easy to determine a coherence "floor" level—the level of coherency below which results are unreliable. This lies at $C_{\rm thr}^2 = 1/N$ when smoothing over N Fourier frequency points. However, attributing such a level is more complicated for wavelet analysis. This arises from smoothing being carried out over both time and scale (i.e., frequency) in the wavelet case, compared to over only frequency in the Fourier instance. The added complexity comes from the variability of the number of points in time over which smoothing is carried out, since the width of the Gaussian profile used in the time smoothing (eq. [2]) has a dependence on η and hence the wavelet scale. An additional problem exists since the filter profile used in time (Gaussian) is smoothly varying and has no explicit number of data points that define the extent of the smoothing, compared to the sharply defined filter used in scale (boxcar).

In the following sections we present and compare two approaches for testing data coherency against the coherence level of noise, initially proposed by Gurley et al. (2003). However, it should be noted that our phase coherence work differs from that of Gurley et al. (2003) in two manners:

1. we apply smoothing in both time and scale, as outlined by Torrence & Webster (1999), rather than just in time;
2. we utilize only the middle time step of the randomized coherence rather than the full transform, as will become apparent in the following section.

3.2.1. *"Mean Floor" Coherency Approach*

In order to understand the expected response of the wavelet coherence to noise (i.e., the floor level), we initially randomized one of the two time series for a large number of realizations. It was noted that a minor difference existed between the mean coherence achieved through randomizing one time series or the other. Because of this, we randomized both time series and calculated the coherence over 10,000 separate realizations. For each of the randomizations performed, we took a slice through the coherence transform at the middle time step. The choice of the middle time step comes from the nature of the wavelet transform, such that this time index coincides with the lowest point of the COI and is thus least affected by edge effects. Also, in Torrence & Compo (1998) wavelet power at the middle time step, averaged over many randomizations of a pure noise time series, was used to successfully show the 2 degree of freedom χ^2 distribution of wavelet power response to noise.

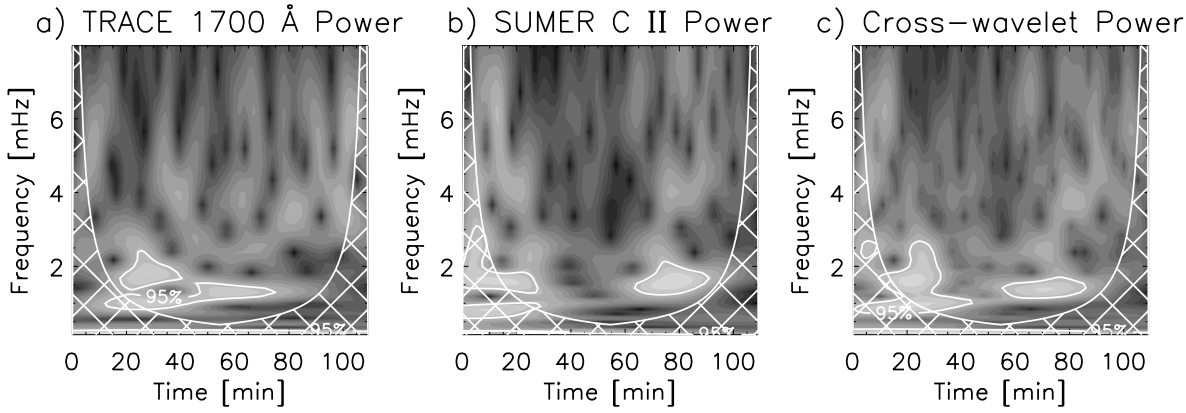

FIG. 6.—Wavelet power transforms for intensity time series of (*a*) *TRACE* 1700 Å and (*b*) SUMER C II 1037 Å, obtained from the magnetic element starting near $x = 182$ in Fig. 3. Plots are shown as a function of time (*abscissa*) and oscillation frequency (*ordinate*). Regions of lighter shading correspond to increased oscillatory power. The crosshatched area marks the COI where edge effects can be important, while the contours show the 95% confidence level. (*c*) Cross–wavelet power transform of (*a*) and (*b*), also contoured at the 95% confidence level. [*See the electronic edition of the Journal for a color version of this figure.*]

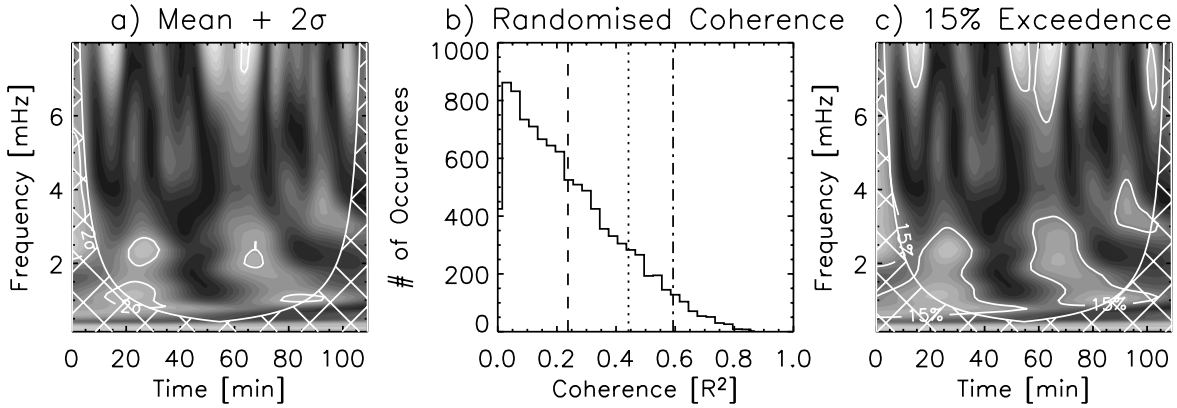

FIG. 7.—(*a*) Wavelet phase coherence transform as a function of time (*abscissa*) and oscillation frequency (*ordinate*), contoured at 2 σ above the mean randomized coherence. Areas of lighter shading have higher coherence. (*b*) Histogram of wavelet randomized coherence values over all 1000 realizations of randomization, for the scale value corresponding to 2.6 mHz. The dashed vertical line denotes the mean, the dashed-dotted line lies 2 σ above this, and the dotted line marks the level above which 15% of the randomized coherence values lie. (*c*) As in (*a*), but contoured at the level above which 15% of the randomized coherence values lie.

The coherence floor level used in data testing can then be taken as the average over all realizations plus some multiple z of the standard deviation of these coherence values:,

$$R^2_{\rm thr}(s) = R^2_{\rm mean}(s) + [zR^2_{\rm stdv}(s)]. \quad (3)$$

In comparison to the general equation for wavelet coherence in Table 1, this shows no n dependence because we take a slice through the coherence transform at a single time step for each realization of the randomization process. This approach yields a value of coherence that varies with scale, with which the

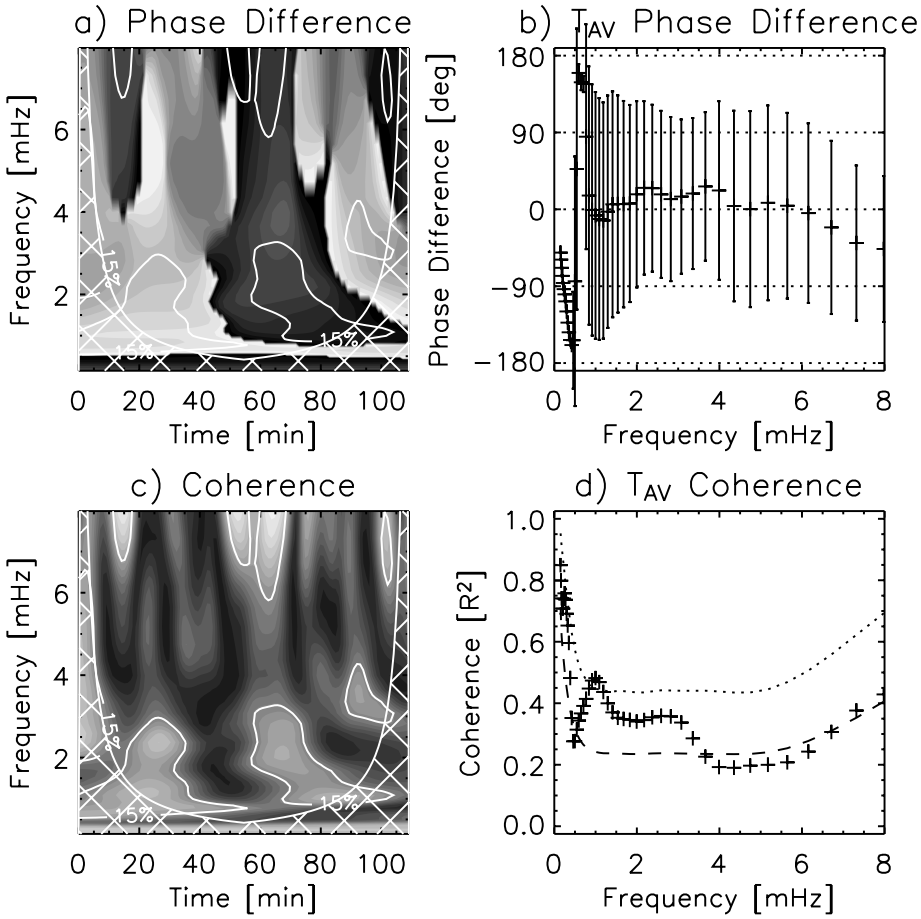

FIG. 8.—(*a*) Full time series wavelet phase difference transform as a function of time (*abscissa*) and oscillation frequency (*ordinate*). Contours overplotted are the 15% coherence exceedence levels, while the crosshatched areas are the COI. (*b*) Time-averaged phase differences (*ordinate*) of (*a*) as a function of oscillation frequency (*abscissa*). Midpoints correspond to the mean temporal phase difference, while the error bars mark out ± 1 σ. (*c*) As in (*a*), but for full time series wavelet phase coherence transform. (*d*) Time-averaged phase coherence (*ordinate*) of (*c*) as a function of oscillation frequency (*abscissa*), where the dotted line marks the 15% coherence exceedence level and the dashed line marks the mean coherence.

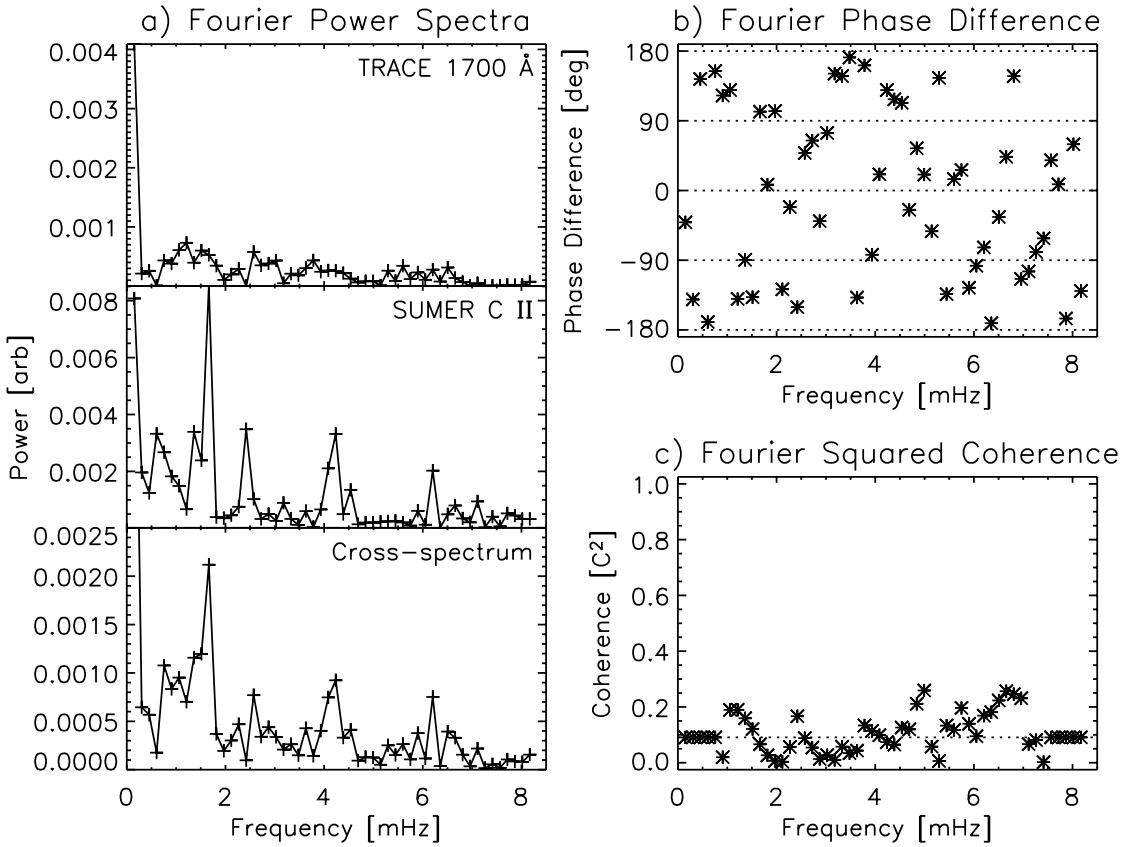

FIG. 9.—(*a*) Full time series Fourier power spectra for the *TRACE* 1700 Å intensity (*top*), SUMER C II intensity (*middle*), and their resulting cross spectrum (*bottom*). (*b*) Fourier phase difference (*ordinate*) shown as a function of frequency (*abscissa*). (*c*) Fourier squared coherence (*ordinate*) shown as a function of frequency (*abscissa*), where the horizontal dotted line denotes the "random" coherence level.

actual data coherence can be contoured at all points in time. An example of this form of thresholding is shown in Figure 7*a*, where $z = 2$ is used in equation (3) (i.e., threshold lying 2 σ above the mean). The subsequent mean and threshold levels used in contouring Figure 7*a*, at the scale value corresponding to 2.6 mHz, are displayed in Figure 7*b* as dashed and dashed-dotted lines, respectively.

3.2.2. *"Floor Exceedence" Coherency Approach*

Alternative thresholding on the distribution of values can be obtained through the construction of a histogram of coherence values obtained in the randomized middle time step approach. Through the inspection of such a histogram, the coherence level above which x% of the randomized samples lie can be easily calculated. Henceforth, this level will be referred to as the x% exceedence level. Real data coherence values lying above this level will have, at most, an x% likelihood of being due to noise. If the histogram is constructed from all randomized coherence values obtained over all scales, this gives a constant value of coherence floor with which to contour the actual data coherence at all points in time and scale. Alternatively, this can be expanded to more closely resemble the previous approach, whereby individual histograms are constructed at each scale value rather than one histogram over all scales. Again, from each individual scale histogram, the coherence level above which x% of the samples lie is taken and applied at that scale through contouring of the actual data coherence. Figure 7*c* displays this method, applied to the same coherence transform as Figure 7*a*. In the histogram of randomized coherence values shown in Figure 7*b*, the 15% exceedence level is marked as a dotted vertical line.

Using the "mean floor" approach shown in § 3.2.1, the threshold level may lie at a coherence value higher than unity for scales showing high mean randomized coherence or for large multiples of σ. Such an outcome is impossible with the "floor exceedence" approach since, by definition, x% of the randomized values will lie above the floor level. Also, the distributions of randomized coherence values at each scale can show significant differences, especially at low frequencies where higher randomized coherence values are prevalent. These facts prompt us to rely more heavily on the scale-dependent floor exceedence approach throughout the remainder of the paper.

3.3. *Phase Difference Analysis*

Measurements of phase difference between two time series yields information on the phase delay between oscillations in the time series as a function of frequency. Through application to data such as that presented here, phase differences show delays experienced in the transfer of oscillatory behavior upward through the solar atmosphere, since the time series have different heights of formation. The wavelet phase difference is calculated in the manner shown in Table 1, where the real and imaginary components of the complex cross–wavelet transform are again used. The range of possible phase difference values is $-180^\circ \leq \phi \leq 180^\circ$, leading to the existence of a 360° discontinuity where phase difference values marginally above 180° are treated as marginally above -180°.

Figure 8*a* displays the wavelet phase difference transform between the *TRACE* 1700 Å and SUMER C II intensities. In this plot absolute white corresponds to 180° and absolute black to -180°, while the contours overlaid are the same

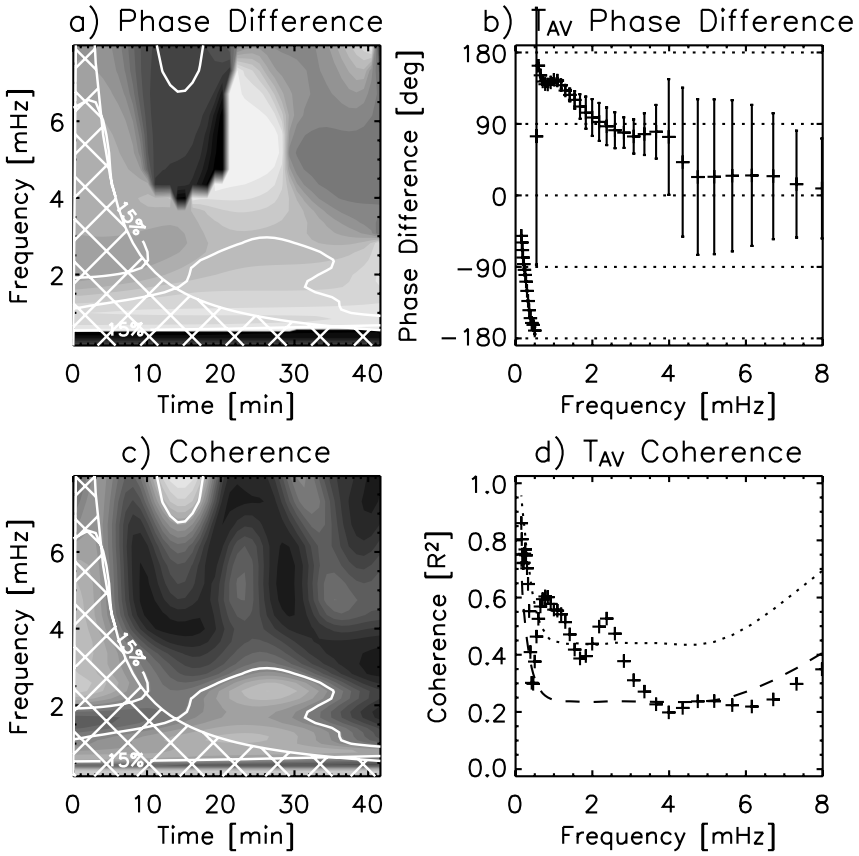

FIG. 10.—Same as Fig. 8, but for the first wave packet (0–42 minutes).

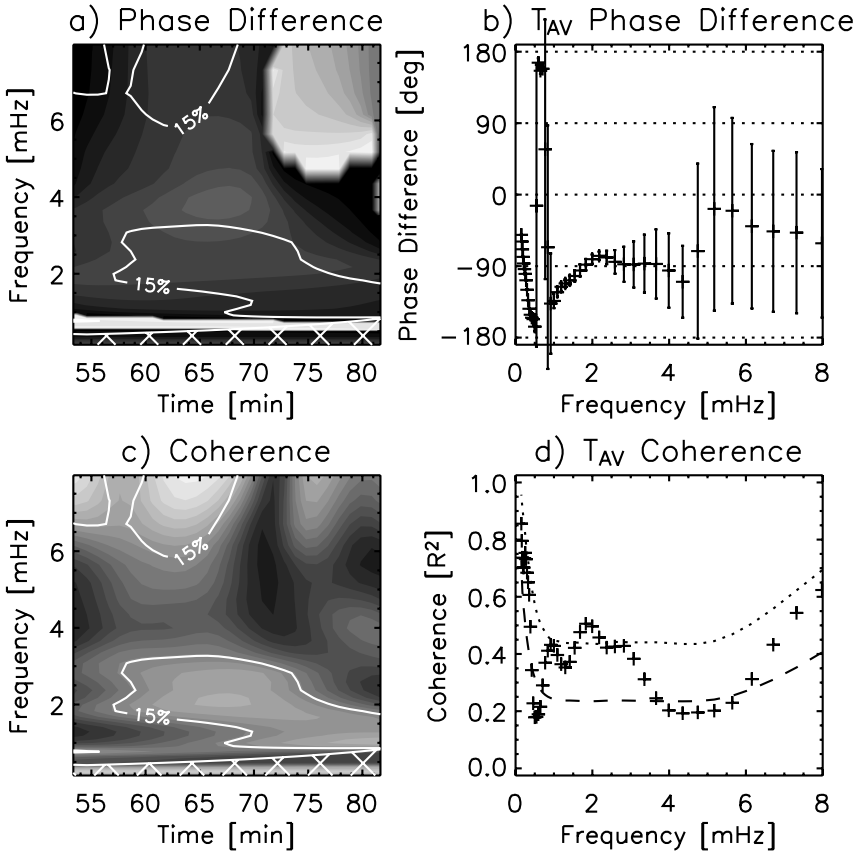

FIG. 11.—Same as Fig. 8, but for the second wave packet (53–81 minutes).

15% exceedence levels of wavelet coherence shown in Figures 7*c* and 8*c*.

4. DISCUSSION

Inspection of Figures 6*a* and 6*b* shows significant power in both the *TRACE* 1700 Å and SUMER C II intensities lying in the 1–3 mHz range, agreeing with earlier observations that network regions predominantly display power below 4 mHz (Lites et al. 1993; McAteer et al. 2002, 2003; Bloomfield et al. 2004). Also, significant power occurs as two distinct wave packets in both plots. Furthermore, the two wave packets are easily distinguished in the cross–wavelet transform of Figure 6*c*, lying mostly outside of the COI. Interestingly, comparison between Figures 6*c*, 8*a*, and 8*c* reveals that the two wave packets occur entirely within separate coherent regions of fairly constant phase difference, on either side of a phase discontinuity. Two further points to note are that

1. the abrupt phase jump separating wave packets occurs over most frequencies at time ~ 52 minutes—similar to the time of emergence of weak neighboring flux mentioned in § 2;
2. another phase jump, back to approximately the same phase values as before, occurs over the frequency range 1.5–5.0 mHz at time ~ 83–87 minutes—slightly before the emergent flux begins moving away from the element under consideration to coalesce with another.

4.1. *Fourier Comparison of Phase Relations*

To compare the information obtained by our wavelet approach to that which Fourier analysis would have yielded, the time-averaged phase differences and coherences were determined. Figure 8*a* shows the wavelet phase difference transform for the entire time series. In this and the following wavelet phase difference plots, the contours mark the 15% coherence floor exceedence as determined in § 3.2.2, correctly displayed in the actual coherence transform of Figure 8*c*. The associated time-averaged values are shown in Figures 8*b* and 8*d* and should be directly comparable to Figures 9*b* and 9*c*. Central dashes on the time-averaged phase difference plots represent the mean temporal phase difference, while the error bars extend to $\pm 1\ \sigma$. The dotted lines in the time-averaged phase coherence plots show the 15% floor exceedence level, while the dashed lines show the mean coherence.

Figure 9*b* shows that Fourier analysis carried out on the entire time series has randomly scattered phase points—comparable to Figure 8*b*, which shows large error bars, with a mean close to 0°. Furthermore, few of the Fourier coherence values in Figure 9*c* lie substantially above the random coherence level of 0.125 (since smoothed over 8 frequency points), nor do they show any grouping together, leading to the interpretation of a lack of coherence. Again, Figure 8*d* is in good agreement with this result, showing nearly all time-averaged coherence values lying below the 15% exceedence level.

Closer inspection of the first wave packet (0–42 minutes; Fig. 10) shows a decreasing positive phase difference ($\sim 150^\circ \rightarrow 90^\circ$) when moving through the frequency range 0.5–3 mHz in Figure 10*b*, while Figure 10*d* tells us that the time-averaged coherence over 0.5–1.5 and 2.0–2.8 mHz lies marginally above the 15% exceedence level.

Similarly, for the second wave packet (53–81 minutes; Fig. 11), there appears to be a fairly constant negative phase difference ($\sim -110^\circ \rightarrow -90^\circ$) over the range 1.5–4 mHz in Figure 11*b*. However, this wave packet shows a slightly more significant phase coherence than the previous one, rising higher above the 15% exceedence level over the range 1.5–2.5 mHz in Figure 11*d*. Because of the 360° ambiguity, this negative phase difference may be alternatively interpreted as $\sim 250^\circ$–270°.

5. CONCLUSIONS

Wavelet analysis is an improved tool over that of classical Fourier analysis for studying temporal relations. This paper has extended the already versatile wavelet analysis tool into the area of phase coherence studies.

In the example presented here, both wave packets observed on either side of a phase discontinuity show slightly varying, nonzero phase differences over a range of frequencies ($\sim$1–4 mHz). The change from $\sim 90^\circ$–150° to $\sim -90^\circ$–-110° (alternatively $\sim 250^\circ$–270°) may indicate either an increase or decrease in phase delay between the respective atmospheric heights, since the direction of the change in phase difference is not discernible. This occurs when a weak flux element emerges close to the element under consideration and reverts to roughly the previous values as it passes away.

By way of investigation, the local magnetic field inclination angle as measured by the ASP is shown in Figure 12. In this diagram, local field inclinations of 0° (i.e., vertical to the solar

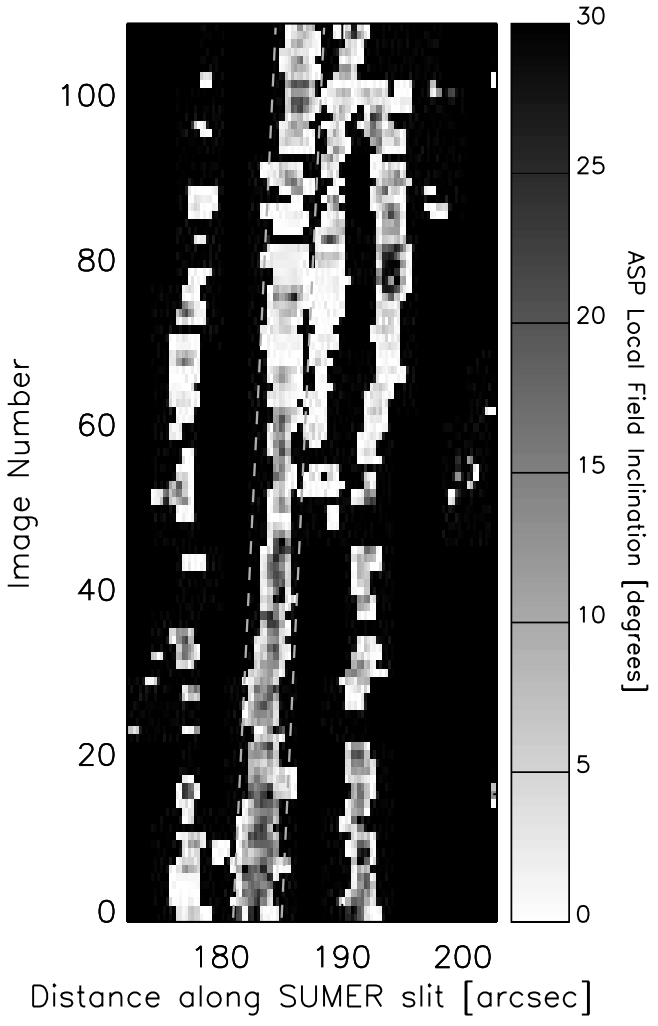

FIG. 12.—Spacetime plot showing ASP local photospheric magnetic field inclination angle (same spatial and temporal coverage as in Fig. 4). Pixels not inverted by the ASP software and those with inclination angles larger than 30° have been clipped to show fine detail in the values near 0°. Dashed lines again mark the spatial region over which intensity time series were extracted. [*See the electronic edition of the Journal for a color version of this figure.*]

surface) are shown as pure white, pixels not inverted by the ASP reduction software have been set to pure black, and values greater than 30° have been clipped to increase the contrast of those values around 0°. From this it appears that the magnetic topology has indeed changed, such that the field lines associated with the magnetic element have become less inclined (i.e., more vertical) by the presence of this neighboring, same-polarity element. This leads us to the conclusion that the change in phase difference between the first and second wave packets is due to a decrease in phase delay, since the path length experienced by waves propagating between two separate heights of formation will be shorter for more vertical inclinations (assuming a roughly plane-parallel atmospheric geometry).

Future work will consist of better determining the method required for attributing a floor level to the wavelet coherence transform, allowing a better comparison with previous Fourier phase coherence studies. Application of this technique to other atmospheric parameters, such as Doppler velocities, will be extremely beneficial.

This work has been supported by the UK Particle Physics and Astronomy Research Council. D. S. B. is supported by a Northern Ireland Department for Employment and Learning studentship. J. M. A. was supported by the Leverhulme Trust via grant F/00203/A and is currently funded by a National Research Council Research Associateship. B. W. L. was supported in part by NASA *SOHO* Guest Investigator Award W-19,328. F. P. K. is grateful to A. W. E. Aldermaston for the award of a William Penney Fellowship. The authors extend their thanks to C. Torrence for useful discussion on wavelet analysis, and to the anonymous referee for comments that helped increase the clarity of the final article.

REFERENCES

Bloomfield, D. S., McAteer, R. T. J., Mathioudakis, M., Williams, D. R., & Keenan, F. P. 2004, ApJ, 604, 936
De Moortel, I., Ireland, J., & Walsh, R. W. 2000, A&A, 355, L23
De Pontieu, B., Erdélyi, R., & de Wijn, A. G. 2003, ApJ, 595, L63
Gibson, E. G. 1973, The Quiet Sun (NASA SP-303; Washington: NASA)
Gurley, K., Kijewski, T., & Kareem, A. 2003, J. Eng. Mech., 129, 188
Judge, P. G., Tarbell, T. D., & Wilhelm, K. 2001, ApJ, 554, 424
Lites, B. W., Rutten, R. J., & Kalkofen, W. 1993, ApJ, 414, 345
McAteer, R. T. J., Gallagher, P. T., Williams, D. R., Mathioudakis, M., Bloomfield, D. S., Phillips, K. J. H., & Keenan, F. P. 2003, ApJ, 587, 806
McAteer, R. T. J., Gallagher, P. T., Williams, D. R., Mathioudakis, M., Phillips, K. J. H., & Keenan, F. P. 2002, ApJ, 567, L165
Skumanich, A., & Lites, B. W. 1987, ApJ, 322, 473
Torrence, C., & Compo, G. P. 1998, Bull. Am. Meteorol. Soc., 79, 61
Torrence, C., & Webster, P. J. 1999, J. Climate, 12, 2679
Williams, D. R., et al. 2001, MNRAS, 326, 428